Coupling WOFOST and HYDRUS-1D to simulate daily maize growth, water– salt dynamics and stress responses under salinity gradients in salinized farmland

Jing Zhang
Ningxia University
Xiaojing Shen
sxj15191418250@126.com
Ningxia University
Run Wu
Ningxia University
Jingyu Ji
Ningxia University
Fenjie Shang
Ningxia University

Research Article

Keywords: WOFOST model, HYDRUS-1D model, salt stress, soil water–salt transport, Richards equation, Maas–Hoffman function, inter-annual validation

Posted Date: March 20th, 2026

DOI: https://doi.org/10.21203/rs.3.rs-9142790/v1

Additional Declarations: No competing interests reported.

Version of Record: A version of this preprint was published at Irrigation Science on August 7th, 2026. See the published version at https://doi.org/10.1007/s00271-026-01157-7.

Coupling WOFOST and HYDRUS-1D to simulate daily maize growth, water–salt dynamics and stress responses under salinity gradients in salinized farmland

Jing Zhang[1] · Xiaojing Shen[2,*] · Run Wu[1] · Jingyu Ji[1] · Fenjie Shang[1]

[1] Lixing College, Ningxia University, Yinchuan 750021, China

[2] School of Civil and Hydraulic Engineering, Ningxia University, Yinchuan 750021, China

* Corresponding author: Xiaojing Shen; E-mail: sxj15191418250@126.com

Abstract

Soil salinization constrains agricultural productivity across approximately 950 million hectares worldwide. In the Yellow River irrigation district of Ningxia, secondary salinization severely depresses maize yields. Existing crop–water–salt models lack day-by-day bidirectional coupling between salt transport and crop growth, over-simplify salt stress representation, and amplify stress through multiplicative integration. To address these gaps, we developed a fully coupled WOFOST–HYDRUS-1D model linking the Richards equation and convection–dispersion equation with crop photosynthesis, transpiration, and assimilate partitioning through a modified Maas–Hoffman function. Salt stress is transmitted via three physiological pathways, and the combined stress factor is computed using Liebig's law of the minimum. The model was calibrated with 43 sampling points spanning low-to-high salinity gradients (1.49–6.79 g kg^{-1}) in Huinong District during 2024, and independently validated with 30 points (1.29–7.75 g kg^{-1}) in 2025. Calibration yielded R^2 = 0.883, RMSE = 0.744 t ha^{-1}, NRMSE = 10.96%, and NSE = 0.795; validation gave R^2 = 0.824, RMSE = 0.753 t ha^{-1}, NRMSE = 11.13%, and NSE = 0.810, confirming strong inter-annual parameter stability. Under high salinity (>4 g kg^{-1}), simulated mean yield declined to 3.75 t ha^{-1}, a 53% reduction compared with low-salinity conditions. Compared with the standard WOFOST model (R^2 = 0.450, RMSE = 1.399 t ha^{-1}), the coupled model substantially improved accuracy.These results show that the coupled model can improve yield prediction under salinity stress and provide a useful tool for irrigation scheduling and water–salt management in salinized farmland.

Keywords: WOFOST model; HYDRUS-1D model; salt stress; soil water–salt transport; Richards equation; Maas–Hoffman function; inter-annual validation

1 Introduction

Soil salinization is a major environmental challenge in arid and semi-arid regions, affecting approximately 950 million hectares globally and 36 million hectares in China (Haj-Amor et al. 2022). In the Yellow River irrigation district of Ningxia, prolonged flood irrigation has raised groundwater tables and intensified evaporative salt accumulation, causing secondary salinization to worsen progressively (Li et al. 2022a). Topsoil salt contents exceeding 7 g kg^{-1} have been recorded in some fields, with maize yield reductions of more than 50% (Wang et al. 2024). Developing coupled simulation models that accurately capture the dynamic interactions among soil water, salts, and crop growth is therefore essential for guiding irrigation optimization and saline-land reclamation.

Research on crop–water–salt coupled models dates to the 1970s. Maas and Hoffman (1977) proposed the classical salinity–yield threshold–slope function that remains the theoretical cornerstone of this field. The WOFOST (World Food Studies) model, developed at Wageningen University, is a widely validated process-based crop growth model (de Wit et al. 2019; Van Keulen and Wolf 1986) with extensive applications in regional yield prediction (Zhang et al. 2026). HYDRUS-1D, with its robust numerical solution of the Richards equation and flexible solute transport capabilities, has become the standard international tool for soil water–salt simulation (Šimůnek et al. 2016; Šimůnek et al. 2008). However, each model alone has inherent limitations: WOFOST lacks a mechanistic description of soil water–salt processes, whereas HYDRUS-1D cannot simulate crop growth or its feedback on soil water–salt dynamics (Wang et al. 2017).

Several studies have coupled these two models. Zhou et al. (2012) first linked HYDRUS-1D with WOFOST for wheat irrigation simulation in semi-arid northwest China, establishing the basic coupling framework. Li et al. (2012) extended the approach to maize irrigation, confirming its applicability in arid environments. Hao et al. (2015) applied a distributed HYDRUS–EPIC framework to simulate soil water–salt dynamics and crop yield in the Hetao irrigation district, identifying soil salinity as the primary yield-limiting factor. Huang et al. (2017) used WOFOST for dynamic simulation of winter wheat growth across major Chinese production regions, and Cai et al. (2019) determined WOFOST parameters for spring maize at Jinzhou, providing a reference for model localization. More recently, Tian et al. (2025) assimilated Sentinel-1/2 remote sensing data into the WOFOST–HYDRUS coupled model via ensemble Kalman filtering, achieving centimeter-resolution root-zone soil moisture estimation, and Zhao et al. (2025) simulated apple-tree water deficit with an improved WOFOST–HYDRUS model (LAI R^2 = 0.89–0.95). In the area of salinization management, Chen et al. (2022) coupled HYDRUS-2D with SWAP–WOFOST (van Dam et al. 2008) to optimize winter irrigation for salinized farmland, and Li et al. (2023) combined HYDRUS (2D/3D) with stable isotope methods to quantify water–salt transport pathways. Miao et al. (2025) integrated APSIM with deep learning for yield simulation in saline–alkaline land (R^2 = 0.9) but noted that existing models still lack adequate coupling of osmotic stress. Chevuru et al. (2025) demonstrated through bidirectional coupling of PCR-GLOBWB 2 and WOFOST that bidirectional feedback mechanisms significantly improve simulation accuracy in shallow-groundwater regions.

Despite this progress, important gaps remain. First, most WOFOST–HYDRUS coupling studies have focused on water stress and have not yet achieved day-by-day dynamic bidirectional coupling of salt transport and crop growth (Zhou et al. 2012; Li et al. 2012; Tian et al. 2025; Zhao et al. 2025). Second, salts affect crops through multiple pathways—osmotic effects, ion toxicity, and disrupted assimilate partitioning (Maas and Hoffman 1977; Munns and Tester 2008)—yet existing models mostly represent these with a single reduction function. Third, multiple stresses are commonly integrated multiplicatively, which excessively amplifies effects under high-salinity conditions (Siad et al. 2019). Fourth, most models lack independent inter-annual validation, limiting assessment of parameter stability and generalizability (Zhang et al. 2026; Jin et al. 2023).

This study addresses the following central question: how to achieve dynamic bidirectional coupling of soil water–salt transport and crop growth at a daily time step, and how to simulate maize yield responses under saline conditions through multi-pathway stress mechanisms. We constructed a fully coupled WOFOST–HYDRUS-1D model incorporating a three-pathway stress mechanism—photosynthesis, transpiration, and assimilate partitioning—based on a modified Maas–Hoffman function, with Liebig's law of the minimum for stress integration. Two years of field data (2024 for calibration, 2025 for validation) were used to evaluate model accuracy and inter-annual parameter stability in salinized maize farmland in Huinong District, Ningxia.

The objectives of this study were to: (i) develop a daily bidirectionally coupled WOFOST–HYDRUS-1D model for simulating maize growth and soil water–salt dynamics under saline conditions; (ii) incorporate a three-pathway salt stress mechanism affecting photosynthesis, transpiration, and assimilate partitioning; and (iii) evaluate model performance and inter-annual parameter stability using two years of field observations in the Yellow River irrigation district of Ningxia. Furthermore, we analyzed the simulated water–salt dynamics and stress patterns across salinity gradients to discuss the implications of the current irrigation regime and identify potential directions for irrigation optimization.

2 Materials and methods

This study did not involve human participants or animals. All field experiments were conducted on agricultural land with proper authorization.

2.1 Study area

The study area is located in Lihe Township, Huinong District, Shizuishan City, Ningxia Hui Autonomous Region (106°42′–107°10′ E, 38°50′–39°25′ N), at the northern end of the Yinchuan Plain on the Yellow River alluvial floodplain, at elevations of 1090–1110 m a.s.l. The area has a mid-temperate continental arid climate: mean annual temperature 8.4 °C (July mean 23.5 °C, January mean −9.8 °C), accumulated temperature above 10 °C of 3200–3400 °C·d, and a frost-free period of 150–170 d, supporting a single maize crop per year. Mean annual precipitation is 180–200 mm, with over 60% falling between July and September. Annual pan evaporation reaches 1800–2000 mm, yielding an evaporation-to-precipitation ratio exceeding 9; agricultural production depends entirely on Yellow River diversion irrigation.

The predominant soil type is irrigated alluvial soil with loam texture, pH 7.8–8.5, organic matter 12–18 g kg^{-1}, bulk density 1.35–1.45 g cm^{-3}, field capacity 0.28–0.32 cm^3 cm^{-3}, and wilting point 0.14–0.18 cm^3 cm^{-3}. The dominant salt type is sulfate–chloride, with Na^+, Ca^{2+}, SO_4^{2-}, and Cl^- as the principal ions. Prolonged flood irrigation has raised the groundwater table to depths of 1.5–3.0 m (as shallow as 1.0 m during spring salt return), driving capillary transport of salts to the surface and creating typical secondary salinization. Considerable spatial variability in salinity across fields provides favorable conditions for studying maize growth responses across salinity gradients.

Maize is the dominant food crop, occupying approximately 40% of cultivated land. It is sown in mid-to-late April and harvested in mid-to-late September (growing period ~150–160 d). In recent years, yield losses from salinization have become increasingly prominent; in some high-salinity fields, actual yields fall below 50% of normal levels, making salt stress the foremost constraint on maize productivity in this district.

2.2 Experimental design and data acquisition

2.2.1 Calibration experiment (2024)

The 2024 field experiment covered approximately 50 ha in Lihe Township, encompassing fields with light, moderate, and severe salinization. The test cultivar was Xianyu 335 (Pioneer 335), widely grown in northwest irrigation districts for its drought resistance and yield stability. Mechanical sowing was performed on 18 April 2024 at 60 cm row spacing and 25 cm plant spacing (~66,700 plants ha^{-1}). Compound fertilizer ($N–P_2O_5–K_2O$ = 26–10–12) was applied as basal dressing at 600 kg ha^{-1}, and urea was top-dressed at 150 kg ha^{-1} at the jointing (early June) and bell (early July) stages. Pest control followed local practice; no significant outbreaks occurred. Harvest was on 18 September (growing period 153 d).

A total of 43 fixed sampling points were established by stratified random sampling, covering fields of different salinity levels. The spatial distribution accounted for micro-topographic variability, soil texture differences, and historical salinization severity. Initial soil salinity (weighted mean of the 0–60 cm profile) ranged from 1.49 to 6.79 g kg^{-1}, divided into three classes: low (<2 g kg^{-1}, $EC_e < \sim 3.2$ dS m^{-1}, $n = 17$), moderate (2–4 g kg^{-1}, EC_e ~3.2–6.4 dS m^{-1}, $n = 16$), and high (>4 g kg^{-1}, $EC_e > 6.4$ dS m^{-1}, $n = 10$).

Each sampling point received four border irrigations during the growing season—at sowing (17 April), jointing (5 June), heading (10 July), and grain filling (5 August)—each at approximately 900 m^3 ha^{-1} (~90 mm), for a seasonal total of ~3600 m^3 ha^{-1} (~360 mm). Soil samples were collected monthly from sowing to harvest at five depths (0–20, 20–40, 40–60, 60–80, and 80–100 cm), with two replicates per layer. Soil water content was determined gravimetrically (oven-dried at 105 °C, precision ±0.5%), and soil salt content was measured by electrical conductivity of a 5:1 water-to-soil extract (DDSJ-318 conductivity meter), converted to mass salt content via a site-specific empirical relationship. At harvest, yield was determined by five-point sampling (five 2 m^2 quadrats per point), with grain moisture standardized to 14%. Yield components (ear length, kernels per ear, grain weight) and auxiliary indicators (aboveground biomass, harvest index) were also recorded.

2.2.2 Validation experiment (2025)

In 2025, 30 fixed sampling points were established in the same study area: 12 in low-salinity, 11 in moderate-salinity, and 7 in high-salinity fields. Initial salinity (0–60 cm weighted mean) ranged from 1.29 to 7.75 g kg^{-1}. The cultivar, sowing method, fertilization, irrigation schedule, and data collection procedures were identical to 2024. Total growing-season precipitation was 178 mm and effective accumulated temperature was 1782 °C·d, both close to multi-year averages (169 mm and ~1800 °C·d). The 2025 data were used exclusively for independent validation, with no parameter adjustment, to objectively assess cross-year generalization.

2.2.3 Meteorological data

Daily meteorological data were obtained from Huinong District meteorological station (station no. 53614, ~5 km from the experimental area) and subjected to quality control and gap-filling. Variables included daily maximum and minimum temperatures (T_{max}, T_{min}), mean temperature (T_{mean}), precipitation (P), sunshine hours (n), 2 m wind speed (u_2), relative humidity (RH), and solar radiation (R_s). Reference crop evapotranspiration (ET_0) was calculated with the FAO-56 Penman–Monteith equation (Allen et al. 1998):

$$ET_0 = [0.408\Delta(R_n - G) + \gamma(900/(T + 273))u_2(e_s - e_a)] / [\Delta + \gamma(1 + 0.34u_2)] \quad (1)$$

where R_n is net radiation (MJ m^{-2} d^{-1}); G is soil heat flux (approximated as zero at daily scale); e_s and e_a are saturation and actual vapor pressures (kPa); Δ is the slope of the saturation vapor pressure–temperature curve (kPa $°C^{-1}$); and γ is the psychrometric constant (kPa $°C^{-1}$). During the 2025 growing season (18 April–18 September), T_{mean} = 19.8 °C, total precipitation = 178 mm, cumulative ET_0 = 846 mm, and cumulative sunshine hours = 1285 h, consistent with multi-year averages (T_{mean} 19.3 °C, precipitation 169 mm, ET_0 851 mm).

Table 1 Summary of field sampling points and conditions in the two-year experiments

Item	**2024 (Calibration)**	**2025 (Validation)**
Total sampling points	43	30
Low salinity (<2 g kg^{-1})	17	12
Moderate salinity (2–4 g kg^{-1})	16	11
High salinity (>4 g kg^{-1})	10	7
Initial salinity range (0–60 cm)	1.49–6.79 g kg^{-1}	1.29–7.75 g kg^{-1}
Sowing date	18 April 2024	18 April 2025
Harvest date	18 September 2024	18 September 2025
Growing period	153 d	153 d

Irrigation events	4 (total 360 mm)	4 (total 360 mm)
Growing-season precipitation	185 mm	178 mm
Effective accumulated temperature	1800 °C·d	1782 °C·d
Data use	Parameter calibration	Independent cross-year validation

2.3 Construction of the WOFOST–HYDRUS-1D coupled model

2.3.1 Overall framework and coupling mechanism

The coupled model is a daily-step simulation system integrating soil physics, solute transport, crop physiology, and agricultural hydrology (Fig. 1). It comprises four core modules: (i) soil water movement (Richards equation, solved by HYDRUS-1D); (ii) salt transport (convection–dispersion equation, solved by HYDRUS-1D); (iii) crop growth (WOFOST algorithms via the Python Crop Simulation Environment, PCSE); and (iv) water–salt stress coupling (modified Maas–Hoffman multi-pathway stress functions). Within each daily time step, the four modules are computed sequentially and exchange information through interface variables, forming a closed dynamic feedback loop.

The coupling mechanism operates bidirectionally. In the forward pathway (soil → crop), HYDRUS-1D outputs daily root-zone mean water content (θ_root) and electrical conductivity (EC_root), from which the stress module calculates salt stress (K_s), water stress (K_w), and combined stress (K_stress) factors; K_stress then modifies WOFOST's daily gross primary productivity (GPP) and assimilate partitioning. In the reverse pathway (crop → soil), WOFOST outputs daily leaf area index (LAI) and root depth (RD), which feed into HYDRUS-1D as inputs for potential transpiration partitioning and root water uptake distribution. WOFOST also provides potential evaporation and transpiration as upper boundary components for HYDRUS-1D. Actual root water uptake, computed by HYDRUS-1D via the Feddes function, enters the

Richards equation as a distributed sink term, dynamically redistributing soil moisture and thereby affecting convective salt transport.

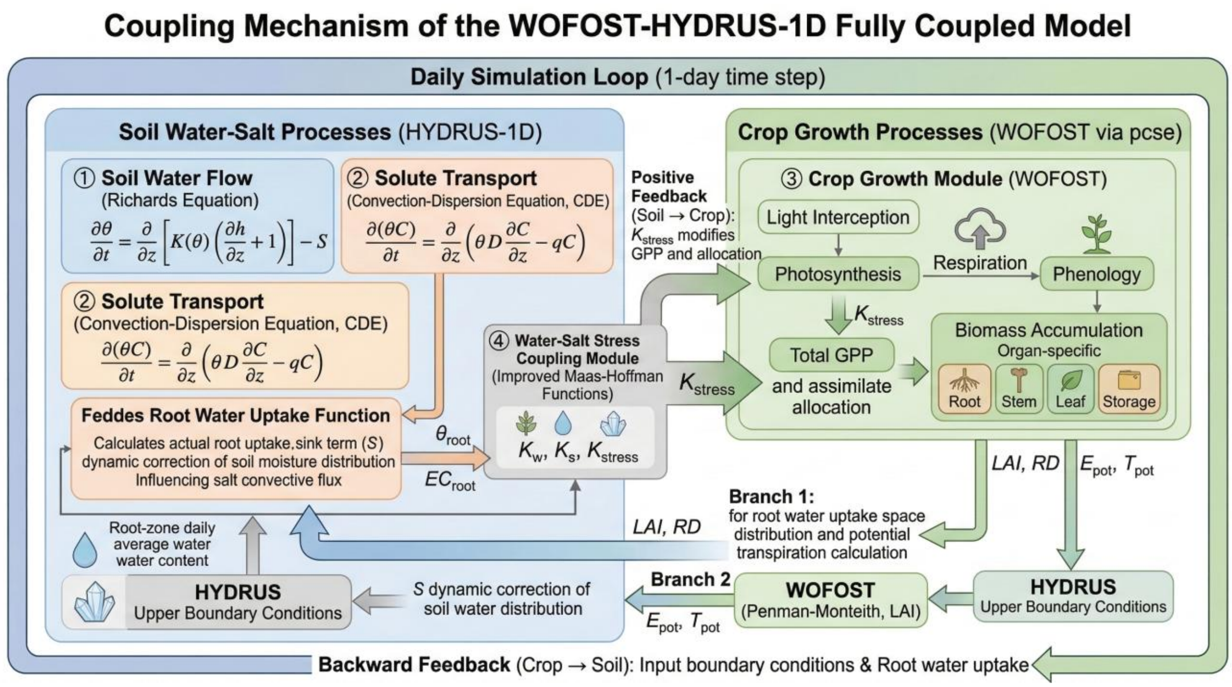

Fig. 1. Model coupling framework

2.3.2 Soil water movement module

Soil water movement is governed by the one-dimensional vertical Richards equation:

$$\partial\theta/\partial t = \partial/\partial z[K(h)(\partial h/\partial z + 1)] - S(z, t) \quad (1)$$

where θ is volumetric water content ($cm^3\ cm^{-3}$); t is time (d); z is soil depth (cm, positive downward from the surface); h is matric potential (cm H_2O); K(h) is unsaturated hydraulic conductivity (cm d^{-1}); and S(z,t) is the root water uptake rate ($cm^3\ cm^{-3}\ d^{-1}$). Soil hydraulic properties were described by the van Genuchten–Mualem (VGM) model (van Genuchten 1980; Mualem 1976):

$$\theta(h) = \theta_r + (\theta_s - \theta_r)/[1 + |\alpha h|^n]^m (h < 0) \quad (2)$$

$$K(h) = K_s \cdot S_e^l \cdot 1 - [1 - S_e^{(}1/m)]^{m2} \tag{3}$$

$$S_e = (\theta - \theta_r)/(\theta_s - \theta_r) \tag{4}$$

where θ_r and θ_s are residual and saturated water contents; α is the inverse air-entry value (cm^{-1}); n is the pore-size distribution parameter; $m = 1 - 1/n$; K_s is saturated hydraulic conductivity ($cm\ d^{-1}$); S_e is effective saturation; and $l = 0.5$ (Mualem 1976). The 0–100 cm profile was discretized into five 20 cm layers and solved by the Galerkin finite element method. The upper boundary was atmospheric (infiltration and evaporation governed by precipitation, irrigation, and potential evaporation); the lower boundary was free drainage ($\partial h/\partial z = 0$ at 100 cm).

2.3.3 Salt transport module

Salt transport follows the one-dimensional convection–dispersion equation (CDE):

$$\partial(\theta c)/\partial t = \partial/\partial z[\theta D(\theta, v) \cdot \partial c/\partial z] - \partial(qc)/\partial z - S_s(z, t) \tag{5}$$

where c is soil solution salt concentration ($g\ L^{-1}$); $D(\theta,v)$ is the hydrodynamic dispersion coefficient ($cm^2\ d^{-1}$); q is water flux ($cm\ d^{-1}$); and $S_s = S \cdot c$ is the root salt uptake rate (passive uptake assumed). The dispersion coefficient is:

$$D(\theta, v) = D_m \cdot \tau(\theta) + \lambda_L \cdot |v| \tag{6}$$

where D_m is the molecular diffusion coefficient (~1.6 $cm^2\ d^{-1}$ for NaCl at 25 °C); $\tau(\theta)$ is the tortuosity factor (Millington–Quirk model); λ_L is longitudinal dispersivity (5 cm); and $v = q/\theta$ is pore-water velocity. Salt concentration was converted to saturated paste extract EC_e via:

$$EC_e = \kappa \cdot c \tag{7}$$

where κ = 1.6 dS·L m^{-1} g^{-1}, consistent with literature values for sulfate–chloride soils in Huinong (1.5–1.8). The upper salt boundary was Cauchy-type, with influent concentration set by the flux-weighted average of irrigation water (EC ≈ 0.5 dS m^{-1}) and precipitation. The lower boundary was zero-concentration-gradient. Initial salt profiles were prescribed from pre-sowing measurements.

2.3.4 Root water uptake module

Root water uptake S(z,t) was computed using the Feddes et al. (1978) model:

$$S(z,t) = \alpha(h) \cdot b(z) \cdot T_pot \tag{8}$$

where α(h) is a dimensionless water stress function (0–1); b(z) is the normalized root density distribution (cm^{-1}, ∫b(z)dz = 1); and T_pot is potential transpiration (cm d^{-1}). The stress function α(h) follows a piecewise linear form: α = 0 at h ≤ h_4 (wilting point, −8000 cm) or h > h_1 (anaerobiosis, −10 cm); α increases linearly from 0 to 1 between h_4 and h_3 (stress onset: −200 cm at high transpiration, −800 cm at low transpiration); α = 1 between h_3 and h_2 (−25 cm); and α decreases linearly from 1 to 0 between h_2 and h_1. Root density was set as a linearly decreasing function with depth, updated daily according to development stage.

2.3.5 Crop growth module

Crop growth was simulated using WOFOST algorithms implemented through PCSE (Python Crop Simulation Environment). The phenological module drives development through thermal time, expressed by the development stage index DVS (0 at sowing, 1.0 at anthesis, 2.0 at maturity):

$$DVS = \Sigma \max(T_i - T_b, 0)/GDD_req \tag{9}$$

where T_b = 8 °C is the base temperature for maize, and the thermal requirements are TSUM1 = 850 °C·d (sowing to anthesis) and TSUM2 = 950 °C·d (anthesis to maturity). Daily canopy gross primary productivity is calculated by Gaussian integration:

$$GPP = A_{m}ax \cdot f_{r}ad(LAI, R_{s}) \cdot f_{T}(T_{m}ean) \cdot K_{s}tress \quad (10)$$

where A_max is the maximum leaf CO_2 assimilation rate (kg ha^{-1} h^{-1}); f_rad is radiation use efficiency; f_T is a temperature response function (optimum 22–28 °C); and K_stress is the combined stress factor (Section 2.3.6). Net primary productivity (NPP) after deducting maintenance respiration (R_m) is allocated to leaves, stems, roots, and ears according to DVS-dependent partitioning coefficients:

$$NPP = GPP - R_{m} \quad (11)$$

$$R_{m} = \Sigma(RM_{i} \cdot W_{i} \cdot Q_{10}{}^{(}(T - 25)/10)) \quad (12)$$

where RM_i is the maintenance respiration coefficient of the ith organ; W_i is its dry weight; and Q_{10} = 2.0 is the respiration temperature coefficient. Final yield is obtained from WOFOST's storage organ dry weight (WSO) with a grain conversion factor:

$$Y = WSO \cdot f_{g}rain/1000 \quad (13)$$

where Y is grain yield (t ha^{-1}) and f_grain = 0.60, determined from 43 sampling points in which grain dry weight constituted approximately 60% of total storage organ weight. This factor differs from the conventional harvest index (HI = grain/total aboveground biomass); calibrated HI ranged from 0.41 to 0.47, consistent with reported values for maize in northern/northwest China (0.40–0.50).

2.3.6 Water–salt stress coupling module

The water–salt stress coupling module is a key component of the model, designed to represent the effects of salinity on multiple crop physiological processes at a daily time step.

(1) Baseline salt stress function. The salt stress factor K_s follows a modified Maas–Hoffman power function:

$$K_s = \max[1 - b(EC_e - EC_t)]^p, K_min(EC_e > EC_t) \quad (14a)$$

$$K_s = 1(EC_e \leq EC_t) \quad (14b)$$

where EC_e is root-zone weighted mean EC (dS m^{-1}), converted from HYDRUS-1D output via Eq. (8); EC_t is the salinity tolerance threshold (calibrated at 2.15 dS m^{-1}, cf. classical value 1.7); b is the yield decline slope (calibrated at 8.0% per dS m^{-1}, cf. classical 12%); p = 1.50 is a shape parameter producing a convex response curve; and K_min = 0.05 is the lower bound, corresponding to ~5% minimum survival yield.

(2) Three-pathway stress mechanism. Salt stress affects crop growth through three physiological pathways:

Pathway ① Photosynthetic stress (K_ph): Salt induces stomatal closure and ion toxicity (Na^+, Cl^- accumulation in mesophyll cells), suppressing photosynthesis:

$$K_p h = K_s \cdot K_i on \quad (15)$$

Pathway ② Transpiration stress (K_tr): Salt reduces soil solution water potential (osmotic stress) and compounds with soil moisture deficit:

$$K_t r = K_s \cdot K_w \cdot K_o sm \quad (16)$$

Pathway ③ Partitioning stress (K_pa): Under salt stress, crops preferentially allocate resources to roots, reducing the proportion of assimilates directed to storage organs:

$$K_p a = \beta \cdot K_s + (1 - \beta) \quad (17)$$

In these equations: K_{ion} is the ion toxicity factor, declining linearly when EC_e exceeds the ion toxicity threshold $EC_{ion} = 9.0$ dS m^{-1}. K_w is the water stress factor (FAO-56 method): $K_w = 1$ above the depletion threshold $[\theta_{fc} - p\cdot(\theta_{fc} - \theta_{wp})]$, declining linearly to 0 at θ_{wp}, with $p = 0.55$ (FAO recommendation for maize). K_{osm} is the osmotic stress factor: $K_{osm} = 1$ when $EC_e \leq EC_t$; when $EC_e > EC_t$, $K_{osm} = \max(1 - c_{osm}\cdot(EC_e - EC_t), 0)$, with $c_{osm} = 0.01$. $\beta = 0.45$ is the yield coupling coefficient.

(3) Combined stress factor. The combined stress factor is computed using Liebig's law of the minimum:

$$K_s tress = \min(K_p h, K_t r) \times K_p a \tag{18}$$

The limiting-factor approach was preferred over the multiplicative method ($K_{ph} \times K_{tr} \times K_{pa}$) for two reasons. First, photosynthetic and transpiration stresses both reflect limitations on crop water availability; multiplying them would impose a double penalty, overestimating actual stress intensity. Second, under high salinity ($EC_e > 8$ dS m^{-1}), multiplication of multiple stress factors (each <0.5) would drive K_{stress} toward zero, yet field data show that maize can still maintain ~40% of relative yield at $EC_e \approx 10$ dS m^{-1}.

2.4 Model parameter calibration and optimization

2.4.1 Parameter sensitivity analysis

A Sobol variance decomposition (Sobol 1993; Saltelli 2002) was performed on 41 model parameters to identify key parameters and guide calibration. The method yields first-order (S_1) and total-effect (S_T) sensitivity indices; $S_T - S_1 > 0$ indicates parameter interactions. The 41 parameters comprised 22 WOFOST crop parameters (phenological, photosynthetic, respiration, conversion efficiencies, root depth), 7 HYDRUS-1D soil hydraulic parameters (VGM parameters, dispersivity), and 5 salt stress parameters (EC_t, b, p, κ, β). Using Saltelli sampling (N = 1024, total evaluations = 86,016), sensitivity was assessed under two scenarios: potential production (no salt stress, $K_s = 1$) and actual salt-stressed conditions.

2.4.2 Parameter calibration

Calibration targeted the 43 measured yields in 2024, using grid search with sequential parameter optimization (minimizing whole-sample RMSE). Parameters were optimized in order of decreasing S_T. A two-stage strategy was adopted: (i) WOFOST crop parameters were pre-calibrated against yield and biomass from near-salt-free plots (initial EC ≈ 1.0 dS m^{-1}), targeting NRMSE < 15% under stress-free conditions. Key parameters adjusted included TSUM1, TSUM2, AMAX, CVL, and CVO. (ii) With crop parameters fixed, the four most sensitive salt stress parameters (EC_t, b, p, β) were optimized using the full 43-point dataset, sweeping each through its range at fixed steps (EC_t: 0.05 dS m^{-1}; b: 0.2% per dS m^{-1}; p: 0.05; β: 0.05) until convergence (RMSE change < 0.01 t ha^{-1} between rounds).

2.4.3 Independent model validation

Validation used the 30 independent sampling points from 2025 with all parameters fixed at the 2024-calibrated values. The model was driven by 2025 meteorological data and pre-sowing soil water–salt initial conditions, run for 153 d, and simulated yields were compared with measured values.

2.4.4 Localization of WOFOST crop parameters

The default WOFOST maize parameter set was developed for European cultivars and required localization for Xianyu 335. Based on phenological observations from 2024 salt-free plots: TSUM1 was adjusted from 700 to 850 °C·d, and TSUM2 from 850 to 950 °C·d. Maximum photosynthetic rates (AMAX) at mid-to-high development stages were moderately increased following regional literature. Assimilate conversion efficiencies and respiration parameters were kept within literature ranges and fine-tuned during calibration.

2.5 Model evaluation metrics

Six statistical metrics were used for model evaluation:

$$R^2 = \Sigma[(O_i - \bar{O})(P_i - \bar{P})]^2 / \Sigma(O_i - \bar{O})^2 \cdot \Sigma(P_i - \bar{P})^2 \tag{19}$$

$$RMSE = \sqrt{}[\Sigma(P_i - O_i)^2 / n] \tag{20}$$

$$NRMSE = RMSE/\bar{O} \times 100\% \tag{21}$$

$$NSE = 1 - \Sigma(O_i - P_i)^2 / \Sigma(O_i - \bar{O})^2 \tag{22}$$

$$PBIAS = \Sigma(O_i - P_i)/\Sigma O_i \times 100\% \tag{23}$$

$$d = 1 - \Sigma(O_i - P_i)^2 / \Sigma(|P_i - \bar{O}| + |O_i - \bar{O}|)^2 \tag{24}$$

where O_i and P_i are observed and simulated values (t ha^{-1}); $\bar{O}$ is the observed mean; and n is the sample size. NRMSE criteria: <10% excellent, 10–20% good, 20–30% acceptable. NSE: >0.75 good, 0.65–0.75 satisfactory. |PBIAS| < 10%: satisfactory. d (Willmott 1982): >0.90 excellent.

3 Results

3.1 Parameter sensitivity analysis

3.1.1 Potential production scenario

Under stress-free conditions, the most sensitive parameters (S_T > 0.1) were exclusively WOFOST crop parameters (Fig. 2; Table 2): assimilate conversion efficiencies CVL (S_T = 0.193) and CVO (0.192), phenological thermal sums TSUM1 (0.174) and TSUM2 (0.174), maximum photosynthetic rate AMAX (0.151), and initial light use efficiency EFF (0.127). These six parameters collectively explained ~80% of yield variance through their first-order effects, with relatively small interaction effects. All soil hydraulic and salt stress parameters had $S_T < 0.05$, confirming their negligible influence under non-limited conditions.

3.1.2 Salt-stressed scenario

Introducing salt stress fundamentally transformed the sensitivity pattern (Fig. 2; Table 2). Salt stress parameters became the dominant group: EC_t ($S_T = 0.286$) and b (0.240) ranked first and second, followed by p (0.188) and β (0.152). The total-effect indices of these four parameters summed to 0.866, indicating near-complete dominance over yield variance. Among crop parameters, CVO (0.210) and CVS (0.210) maintained high sensitivity; TSUM1 (0.131) and TSUM2 (0.138) declined but remained above the threshold; and TBASE (0.100) became newly sensitive because base temperature affects the rate of thermal accumulation and hence the duration of salt exposure. Photosynthetic (AMAX, EFF) and respiration parameters decreased substantially ($S_T < 0.08$), confirming that under saline conditions, yield is governed by stress severity rather than photosynthetic capacity.

These results validate the staged calibration strategy: under salinized conditions, salt stress parameters are the primary determinants of yield prediction accuracy, whereas under non-salinized or mildly salinized conditions, cultivar physiological parameters—particularly conversion efficiencies and thermal sums—dominate.

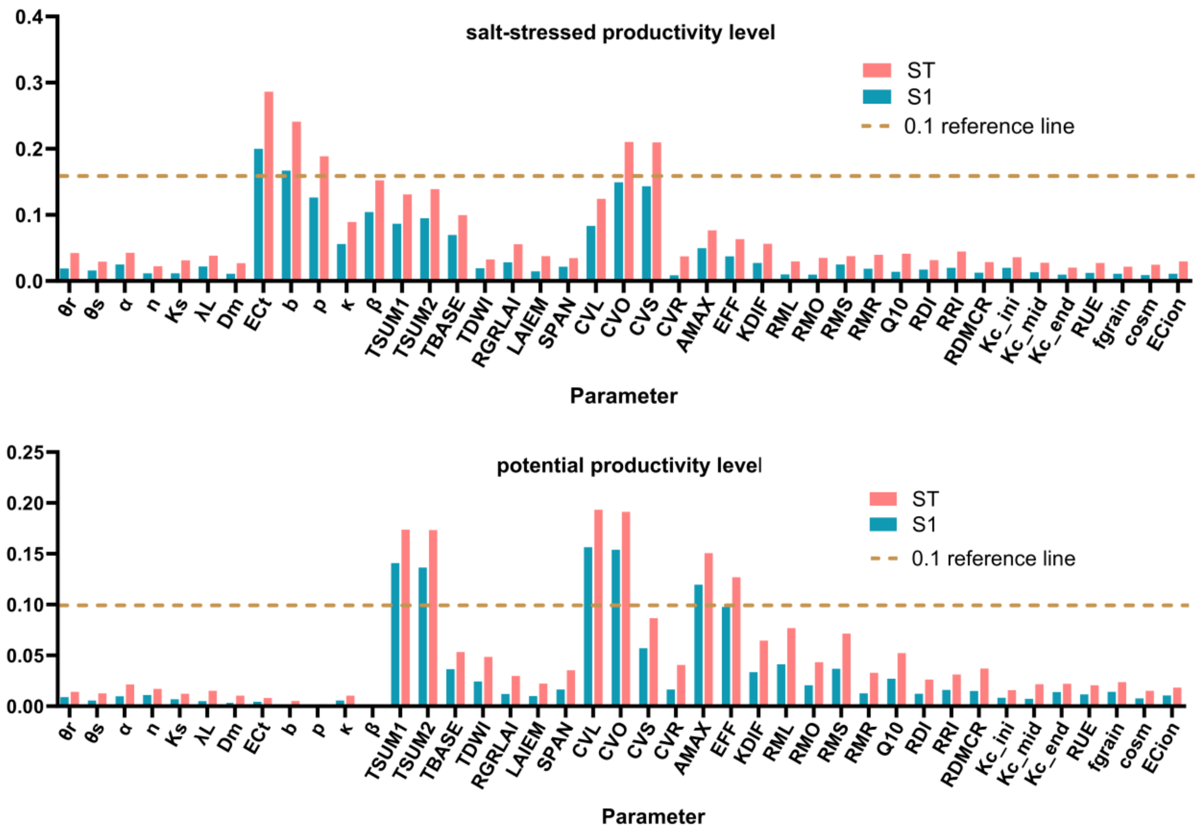

Fig. 2. Sensitivity analysis of key model parameters under potential production and salt-stressed scenarios.

Table 2 Highly sensitive parameters (S_T > 0.1) under potential production and salt stress scenarios

Parameter	**Category**	**Potential S_T**	**Salt stress S_T**	**Change**
EC_t (salinity threshold)	Salt stress	0.008	0.286	↑ Sharp increase
b (yield decline slope)	Salt stress	0.005	0.240	↑ Sharp increase
p (shape parameter)	Salt stress	0.003	0.188	↑ Sharp increase
β (yield coupling coeff.)	Salt stress	0.002	0.152	↑ Sharp increase
CVL (leaf conversion eff.)	Crop growth	0.193	0.124	↓ Decreased
CVO (storage organ	Crop growth	0.192	0.210	→ Stable

conv.)				
CVS (stem conversion eff.)	Crop growth	0.087	0.210	↑ Increased
TSUM1 (vegetative thermal)	Crop growth	0.174	0.131	↓ Decreased
TSUM2 (reproductive thermal)	Crop growth	0.174	0.138	↓ Decreased
TBASE (base temperature)	Crop growth	0.053	0.100	↑ Newly sensitive
AMAX (max. photosyn. rate)	Crop growth	0.151	0.076	↓ Sharp decrease
EFF (light use efficiency)	Crop growth	0.127	0.064	↓ Sharp decrease

3.2 Growing-season process simulation

3.2.1 Root-zone water dynamics

The model simulated daily root-zone water content throughout the 153-d growing season. Root depth expanded progressively from 10 cm at emergence to 80 cm at ~47 d after emergence; accordingly, θ_{root} represents a dynamically evolving depth window. All salinity classes in both years exhibited consistent water dynamics (Fig. 3). Following pre-sowing irrigation, root-zone θ reached 0.298–0.334 cm^3 cm^{-3}, near or slightly above field capacity (θ_{fc} = 0.28–0.32 cm^3 cm^{-3}). Water content declined rapidly during the first 20–40 d with increasing crop demand, reaching the first seasonal trough (0.22–0.24 cm^3 cm^{-3}) by the jointing stage (~40 DAS). Irrigation then restored θ to 0.23–0.28 cm^3 cm^{-3} during jointing to heading (60–80 DAS). A second trough (0.217–0.230 cm^3 cm^{-3}) appeared at early grain filling (~100 DAS), followed by recovery to

0.273–0.299 cm³ cm⁻³ after the final irrigation (~120 DAS). During late grain filling to maturity, θ stabilized at 0.25–0.27 cm³ cm⁻³.

Season-mean θ_root was highly consistent between years: 0.264–0.269 cm³ cm⁻³ in 2024 and 0.268–0.271 cm³ cm⁻³ in 2025, indicating stable simulation of root-zone water dynamics across different climatic conditions. Notably, mean water content at high-salinity points was slightly higher than at low-salinity points, reflecting lower K_stress, reduced transpiration, and consequently less soil water depletion. This negative feedback—fully captured through the reverse coupling pathway—provides further support for the bidirectional coupling mechanism.In the later growth period (from ~62 DAS), K_w occasionally fell below 1.0 (as low as 0.82), indicating mild water deficit during extended irrigation intervals that formed compound water–salt stress and contributed to accelerated LAI decline. In addition, comparison with field observations showed that the model reasonably captured the timing and magnitude of the main wetting-drying cycles under the border-irrigation regime.

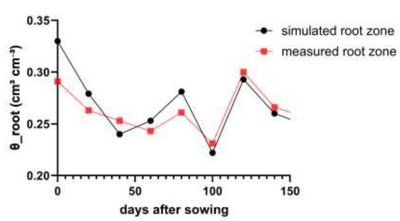

a. 2025 Low-salinity root zone water dynamics

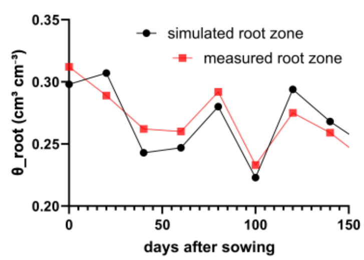

b. 2025 Medium-salinity root zone water dynamic

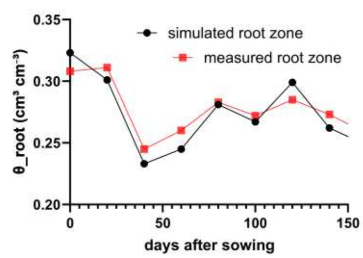

c. 2025 High-salinity root zone water dynamics

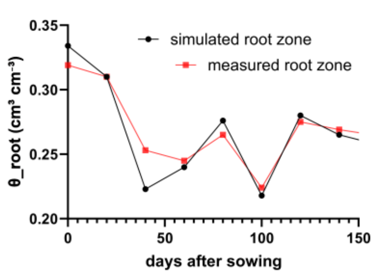

d. 2024 Low-salinity root zone water dynamics

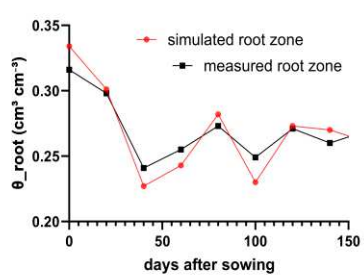

e. 2024 Medium-salinity root zone water dynamics

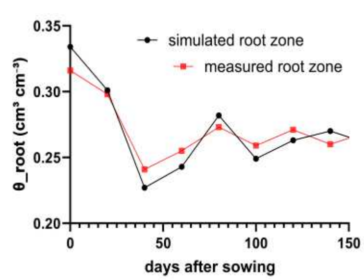

f. 2024 High-salinity root zone water dynamics

Fig. 3. Simulated and observed root-zone soil water dynamics under different salinity levels in 2024 and 2025.

3.2.2 Root-zone salinity dynamics

Root-zone mean EC_e (0–80 cm) exhibited pronounced stage-dependent fluctuations under the interacting effects of initial salinity, irrigation leaching, and evaporative concentration (Fig. 4). Four irrigation events (at ~30, 60, 90, and 120 DAS) served as the primary driver of salt dynamics.

At low-salinity points, initial EC_e was near the tolerance threshold. Taking point 9 as an example (EC_e = 2.15 dS m^{-1} at sowing), evaporative concentration drove a general upward trend, with the growing-season peak (5.0–5.8 dS m^{-1}) occurring during 83–99 DAS. Each irrigation reduced EC_e by ~1.0–1.6 dS m^{-1}, but inter-irrigation evaporative concentration rapidly reversed the effect. By maturity, EC_e reached 4.10 dS m^{-1} (+91% over the initial value), indicating that even initially low-salinity points experience appreciable late-season stress.

At moderate-salinity points, initial EC_e clearly exceeded EC_t. For point 29 (initial EC_e = 3.57 dS m^{-1}), root-zone salinity showed a general declining trend—from 3.57 to 2.23 dS m^{-1} within the first 30 d, continuing to a minimum of 0.98 dS m^{-1} at 120 DAS, and recovering to 2.36 dS m^{-1} at maturity (−34%). Although individual irrigation reductions were modest (0.1–0.6 dS m^{-1}), the cumulative leaching effect significantly improved the growing environment.

At high-salinity points, initial EC_e far exceeded EC_t, imposing severe stress from emergence. For point 22 (initial EC_e = 6.99 dS m^{-1}, surface layer 11.03 dS m^{-1}), root-zone EC_e declined dramatically from 6.99 to 2.63 dS m^{-1} at maturity (−62%). During mid-season (90–130 DAS), EC_e temporarily dropped to 1.0–2.0 dS m^{-1}, reflecting substantial cumulative leaching. The effectiveness of individual irrigations varied: the largest reduction occurred between 59 and 60 DAS (4.11 to 2.23 dS m⁻¹), whereas the reduction at 89–90 DAS was only 0.09 dS m⁻¹, reflecting the influence of pre-irrigation soil moisture and salt status on leaching efficiency.

Two distinct evolution patterns emerged across salinity gradients: low-salinity points, with limited salt reserves, showed net salt increase because leaching could not offset evaporative concentration; moderate- and high-salinity points showed net decrease due to cumulative leaching. Vertically, salt exhibited surface accumulation driven by evaporative capillary rise (e.g., at L09 on day 90, 0–20 cm EC_e = 6.84 vs. 60–80 cm = 1.32 dS m⁻¹). After irrigation, mid-depth layers (20–60 cm) briefly showed increased salt as the wetting front transported salts downward. For high-salinity point H06, surface EC_e decreased from 11.03 to 3.10 dS m⁻¹, with inter-layer differences diminishing, indicating effective attenuation of surface accumulation through sustained leaching. The comparison between simulated and measured salinity dynamics further showed that the model reproduced the main features of salt leaching after irrigation and salt re-accumulation during the inter-irrigation periods.

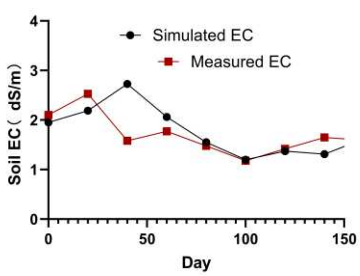

a. 0–20 cm ECe in low-salinity samples

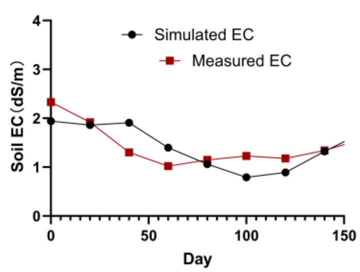

b. 20-40 cm ECe in low-salinity samples

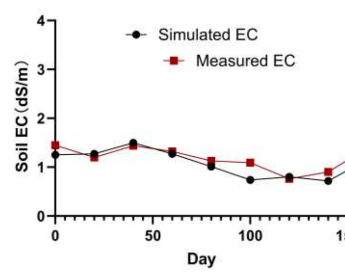

c. 40-60 cm ECe in low-salinity samples

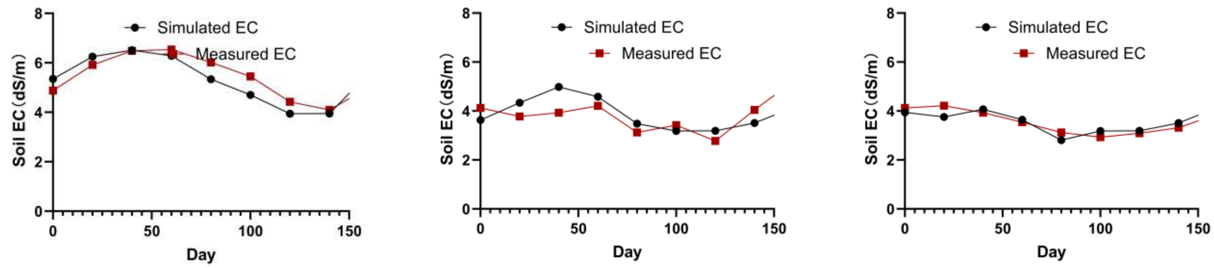

d. 0–20 cm ECe in medium-salinity samples   e. 20-40cm ECe in medium-salinity samples   f. 40-60 cm ECe in medium-salinity samples

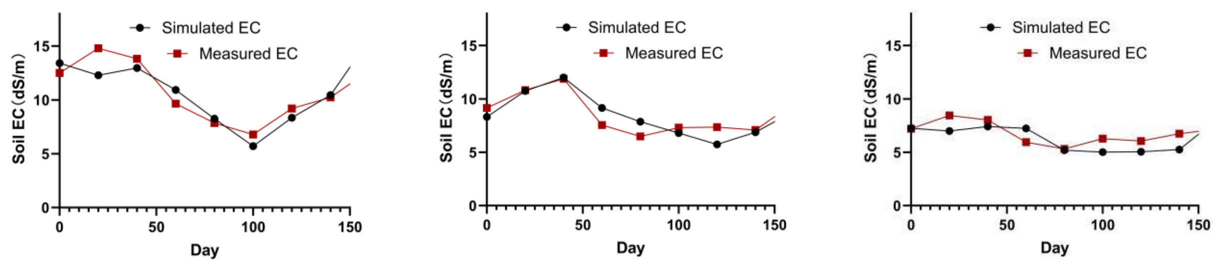

g. 0–20 cm ECe in high-salinity samples   h. 20-40 cm ECe in high-salinity samples   i. 40-60cm ECe in high-salinity samples

Fig. 4. Simulated and observed ECe dynamics in different soil layers under different salinity levels.

3.2.3 Temporal dynamics of the combined stress factor

The temporal dynamics of K_stress link soil water–salt processes to crop growth responses (Fig. 5). Season-mean values were: low salinity 0.91 ± 0.11, moderate salinity 0.74 ± 0.07, and high salinity 0.52 ± 0.08, corresponding to yield losses of ~9%, 26%, and 48%, respectively. At low-salinity points (EC_e 0.8–1.4 dS m^{-1}), K_s remained at 1.0 throughout; yield losses arose solely from occasional water deficit. At moderate-salinity points (EC_e 3.5–4.3 dS m^{-1}), K_stress exhibited a "sawtooth" pattern—dropping to 0.49–0.67 at the end of irrigation cycles and recovering to 0.75–0.78 post-irrigation. At high-salinity points (EC_e 4.5–7.2 dS m^{-1}), K_stress declined progressively (seedling 0.64 → jointing 0.56 → tasseling 0.51 → grain filling 0.46 → maturity 0.41), with post-irrigation peaks also diminishing (seedling 0.60–

0.64 → maturity 0.43–0.44), reflecting the progressive and partly irreversible nature of salt stress.

Under all salinity conditions, a trough occurred during tasseling–silking (61–80 DAS; mean values 0.82, 0.69, and 0.51 for low, moderate, and high salinity), driven by high temperature and transpiration demand combined with root-zone salt accumulation. This period coincides with pollen development and fertilization, during which short-term K_stress drops may have disproportionate effects on kernel number relative to concurrent biomass; however, the current model does not incorporate stage-dependent stress sensitivity weighting. Comparison of K_stress with K_s showed that K_stress/K_s ratios at high- and moderate-salinity points were 0.79 and 0.86, respectively, indicating that water and osmotic stress amplified the combined stress by ~21% and 14% beyond the salt baseline. This amplification was especially pronounced at irrigation cycle ends, supporting the use of the limiting-factor approach in Eq. (20).

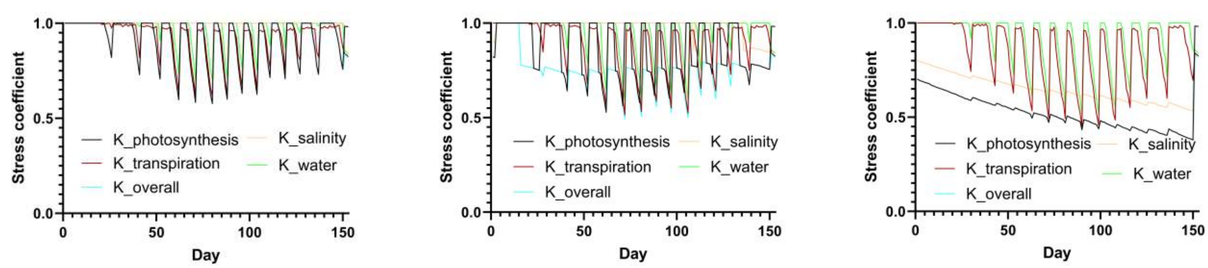

a. Stress coefficient in low-salinity samples b. Stress coefficient in medium-salinity samples c. Stress coefficient in high-salinity samples

Fig. 5. Temporal dynamics of the combined stress coefficient under different salinity levels.

3.2.4 Crop growth process simulation

Simulated LAI dynamics followed a typical unimodal curve, peaking at 80–85 DAS (tasseling–silking). Peak LAI values for low-, moderate-, and high-salinity points were 5.6, 5.1, and 4.0 $m^2\ m^{-2}$, respectively. Differences in peak timing were small, indicating that salt stress primarily reduces the rate of LAI increase rather than altering the phenological pattern. The post-peak decline was notably faster at high-salinity points (~20% more rapid from late grain filling to maturity), consistent with salt-accelerated senescence.

Aboveground biomass (TAGP) followed a typical sigmoid curve. At maturity, TAGP for low, moderate, and high salinity was approximately 16,700, 15,300, and 9,900 kg ha^{-1}, with simulated grain yields of 8.00, 6.89, and 3.75 t ha^{-1} (measured: 8.29 ± 0.36, 6.76 ± 0.81, and 4.16 ± 0.89 t ha^{-1}). At high salinity, TAGP was 59.2% of the low-salinity value, but grain yield was only 46.8%, with yield reduction markedly exceeding biomass reduction (Fig. 6). This discrepancy arises because salt stress not only suppresses photosynthetic production through K_stress but also reduces the proportion of assimilates allocated to storage organs through the partitioning coefficient K_pa. The harvest index decreased from ~0.48 at low salinity to ~0.38 at high salinity, clearly demonstrating the dual suppression pathway of salt stress on yield formation.

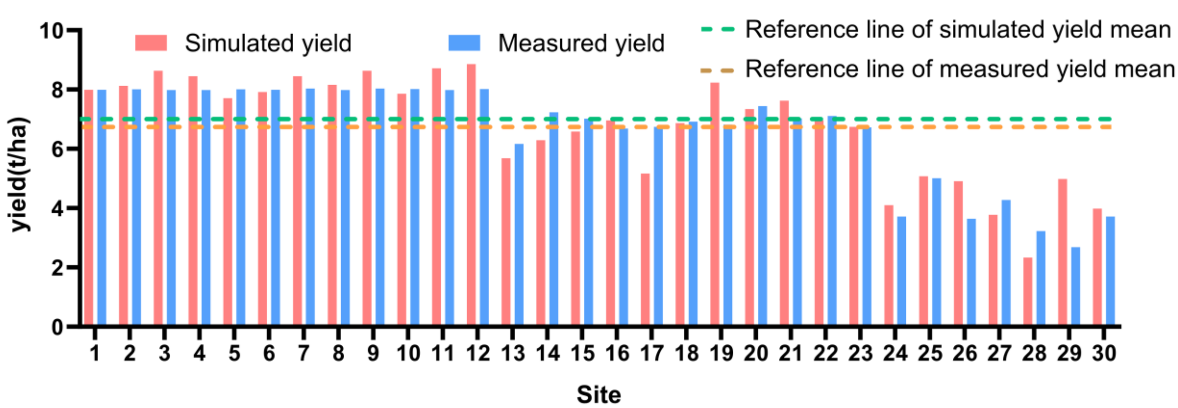

Fig. 6. Comparison between simulated and measured maize yield under different salinity levels.

3.3 Model calibration and validation

3.3.1 Calibration results (2024)

Calibration against 43 sampling points in 2024 (Table 3; Fig. 7) yielded: $R^2 = 0.883$, RMSE = 0.744 t ha^{-1}, NRMSE = 10.96%, NSE = 0.795, PBIAS = +3.39%, MAE = 0.483 t ha^{-1}, and Willmott d = 0.925.

3.3.2 Validation results (2025)

Using the 2024-calibrated parameter set without adjustment, validation against 30 independent points in 2025 gave: $R^2 = 0.824$, RMSE = 0.753 t ha^{-1}, NRMSE = 11.13%, NSE = 0.810, PBIAS = +2.43%, MAE = 0.541 t ha^{-1}, and d = 0.950. Validation accuracy was comparable to calibration accuracy, confirming that the parameters are representative of the study area and showing no evidence of overfitting. Compared with the standard WOFOST model ($R^2 = 0.450$, RMSE = 1.399 t ha^{-1}, NRMSE = 20.68%, NSE = 0.346, PBIAS = −6.99%), the coupled model achieved substantial improvements: R^2 increased by 83%, RMSE decreased by 46%, NSE rose from 0.346 to 0.810, and PBIAS improved from −6.99% to +2.43%.

The consistent positive PBIAS in both years (+3.39% and +2.43%, mean +2.91%) indicates a slight systematic underestimation, which may be related to the model's potential yield parameterization based on multi-year average conditions (~8.5 t ha^{-1}), limiting its capacity to track exceptionally high yields in favorable years. Nonetheless, |PBIAS| < 10% represents acceptable systematic bias.

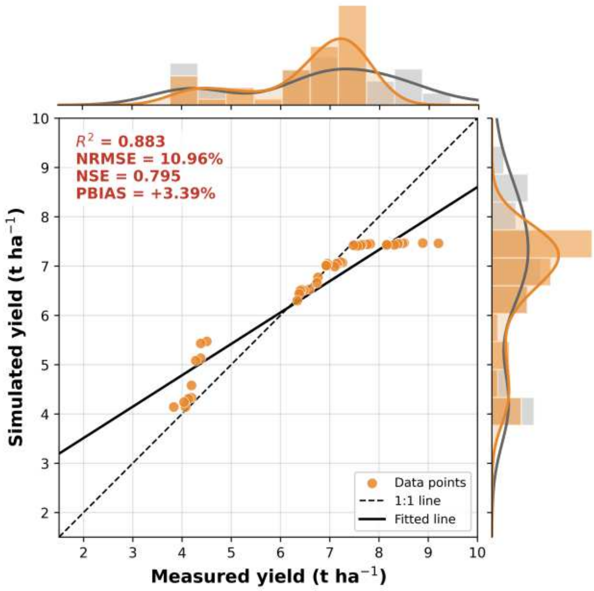

a. Scatter plot of coupled model accuracy (2024)

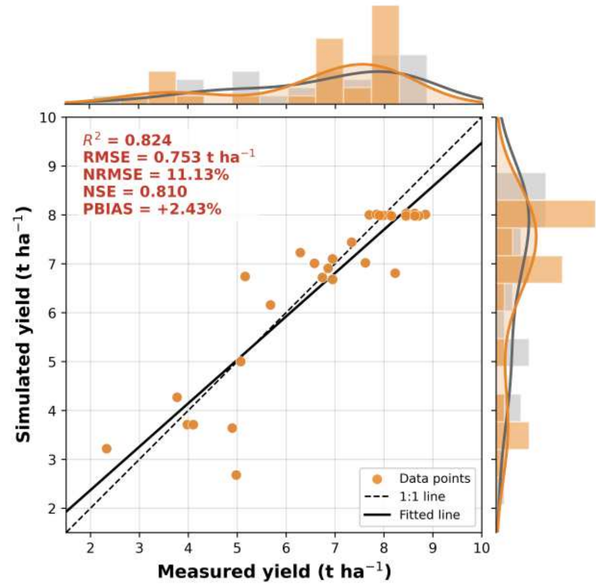

b. Scatter plot of coupled model accuracy (2025)

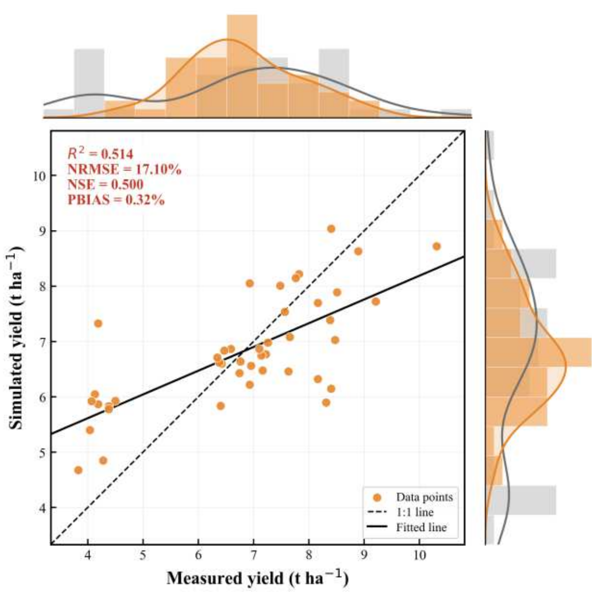

c. Scatter plot of standard WOFOST model accuracy (2024)

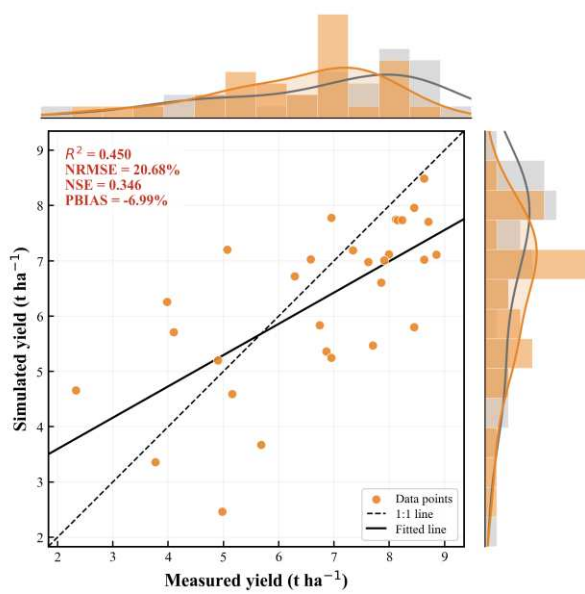

d. Scatter plot of standard WOFOST model accuracy (2025)

Fig. 7. Scatter plots of observed versus simulated maize yield for the coupled and standard WOFOST models in 2024 and 2025.

Table 3 Summary of calibration and validation statistics

Metric	**Symbol**	**Standard WOFOST 2024**	**Standard WOFOST 2025**	**Coupled model 2024 (n=43)**	**Coupled model 2025 (n=30)**

		(n=43)	**(n=30)**		
Coefficient of determination	R^2	0.514	0.450	0.883	0.824
Root mean square error	RMSE (t ha⁻¹)	1.161	1.399	0.744	0.753
Normalized RMSE	NRMSE (%)	17.10	20.68	10.96	11.13
Nash–Sutcliffe efficiency	NSE	0.500	0.346	0.795	0.810
Percent bias	PBIAS (%)	0.32	−6.99	+3.39	+2.43
Mean absolute error	MAE (t ha⁻¹)	0.916	1.163	0.483	0.542
Willmott agreement index	d	—	—	0.925	0.949

4 Discussion

This study developed a fully coupled WOFOST–HYDRUS-1D model to simulate maize yield in salinized farmland of Huinong District, Ningxia. Compared with the standard WOFOST model, the coupled model improved R^2 by 83%, reduced RMSE by 46%, and raised NSE from 0.346 to 0.810, demonstrating the necessity of dynamic water–salt coupling under saline conditions. Previous coupling studies by Zhou et al. (2012) and Li et al. (2012) addressed wheat and maize irrigation but did not incorporate salt stress mechanisms. Miao et al. (2025) achieved higher accuracy (R^2 = 0.9) by combining APSIM with deep learning for saline–alkaline land, though at the cost of reduced interpretability and with acknowledged gaps in osmotic stress coupling. The present study extends the existing WOFOST–HYDRUS framework by introducing a multi-pathway salt stress mechanism and evaluating inter-annual parameter stability through cross-year independent validation in salinized farmland.The necessity of bidirectional coupling received clear empirical support. At high-salinity points, reduced K_stress (mean ~0.52) suppressed transpiration, causing root-zone water content to be paradoxically higher than at low-salinity points. This "salinity suppresses transpiration → root zone retains water" feedback can only be captured within a bidirectional framework; unidirectional coupling would overestimate crop water consumption under high salinity, producing cascading errors. Chevuru et al. (2025) similarly demonstrated that bidirectional feedback improves simulation accuracy in shallow-groundwater regions, consistent with our findings. This negative feedback also exposes a hidden limitation of the current irrigation regime: at high-salinity points, transpiration suppression causes the root zone to retain water, giving the appearance of adequate moisture, yet salt stress persists throughout the season (season-mean K_stress = 0.52). This implies that irrigation scheduling based solely on soil water content is insufficient in salinized farmland; root-zone salinity status must be jointly considered.

The adoption of Liebig's limiting-factor law rather than the traditional multiplicative method for integrating multi-pathway stresses has dual justification. Physically, photosynthetic and transpiration stresses both reflect limitations on crop water availability, and multiplying them imposes a double penalty. Numerically, under high salinity (EC_e > 8 dS m^{-1}), multiple stress factors (each <0.5) multiplied together drive K_stress toward zero, yet field data show maize maintaining ~40% of relative yield at EC_e ≈ 10 dS m^{-1}. The limiting-factor approach avoided this problem effectively: simulated mean yield for high-salinity points was 3.75 t ha^{-1} (measured 4.16 t ha^{-1}), a relative error of only 10%. Siad et al. (2019) likewise noted that multiplicative stress amplification under extreme conditions is a key factor constraining model accuracy. Notably, the K_stress trough was concentrated during tasseling–silking (61–80 DAS), a period that is critical for kernel number determination; the disproportionate yield sensitivity of this window suggests that irrigation timing during this stage may have a far greater impact on final yield than irrigation at other growth stages. Furthermore, the leaching effectiveness of individual irrigations varied dramatically—at high-salinity point H06, the irrigation at 59–60 DAS reduced EC_e by 1.88 dS m^{-1}, whereas the irrigation at 89–90 DAS achieved only 0.09 dS m^{-1}—indicating that irrigation timing may be more important than irrigation amount for salt management in severely affected fields.

The Sobol sensitivity analysis revealed a fundamental transformation of parameter sensitivity between scenarios. Under salt-free conditions, yield variance was primarily explained by crop parameters (CVL, CVO, TSUM1); under salt stress, the four salt parameters (EC_t, b, p, β) dominated with a combined S_T of 0.866. This finding provides theoretical support for the two-stage calibration strategy—constraining crop parameters with salt-free data before optimizing salt parameters with the full dataset. Xing'an et al. (2020) similarly identified CVL, CVO, and TSUM as the most sensitive parameters under stress-free conditions using the EFAST method, further corroborating our results.

Several limitations should be acknowledged. First, the one-dimensional vertical framework cannot represent two- or three-dimensional water–salt transport, limiting applicability for scenarios such as drip irrigation under mulch or subsurface drainage. Second, growth-stage-dependent stress sensitivity has not been fully incorporated; the K_stress trough during tasseling–silking may affect kernel number disproportionately relative to concurrent biomass, and future work could introduce development-stage-specific sensitivity coefficients (Munns and Tester 2008). Third, model performance was evaluated not only against terminal yield but also against observed soil water and salinity dynamics. Comparisons between simulated and measured root-zone water content and soil salinity profiles suggested that the coupled framework was able to reproduce the main temporal patterns of soil water depletion, post-irrigation replenishment, salt leaching, and salt re-accumulation under different salinity conditions. Nevertheless, process-level validation remains incomplete because independent observations were unavailable for several internal crop variables, particularly LAI dynamics, transpiration–evaporation partitioning, and root water uptake distribution. Therefore, further multi-variable validation is still needed before the model can be regarded as comprehensively validated at the process level. Fourth, the two growing seasons studied had climatic conditions close to multi-year averages; performance under extreme years and transferability to other soil types, salt types, or cultivars remain to be tested. Future work should pursue multi-year, multi-site validation to establish the model's regional applicability and temporal robustness.

More broadly, the above analyses indicate that the current uniform four-irrigation schedule is suboptimal across the entire salinity gradient, and salinity-differentiated irrigation management deserves further investigation. The coupled model developed in this study provides a suitable tool for evaluating such alternative irrigation scenarios.

5 Conclusions

(1) The WOFOST–HYDRUS-1D coupled model demonstrated strong simulation accuracy in both calibration (2024, n = 43: R^2 = 0.883, NSE = 0.795) and independent cross-year validation (2025, n = 30: R^2 = 0.824, RMSE = 0.753 t ha^{-1}, NSE = 0.810, d = 0.949), confirming inter-annual parameter stability. Compared with the standard WOFOST model, R^2 improved by 83% and RMSE decreased by 46%, demonstrating the necessity of dynamic water–salt coupling in salinized farmland.

(2) The three-pathway stress mechanism (photosynthesis–transpiration–partitioning), based on the modified Maas–Hoffman function and integrated via Liebig's limiting-factor law, effectively avoided the excessive amplification inherent in multiplicative stress combination under high salinity. The model accurately reproduced yield responses across the full salinity gradient, with a simulated 53% yield reduction under high salinity (>4 g kg^{-1}), consistent with observed trends.

(3) Sobol sensitivity analysis revealed that under salt-free conditions, yield variance is primarily explained by crop physiological parameters (CVL, CVO, TSUM1), whereas under salt stress, four salt parameters (EC_t, b, p, β) dominate with a combined total-effect index of 0.866. This provides theoretical support for the staged calibration strategy of constraining crop parameters before optimizing salt parameters.

(4) The bidirectional coupling mechanism successfully captured the negative feedback whereby salinity suppresses transpiration and the root zone retains water, compensating for a fundamental limitation of unidirectional coupling. The model provides a scientific reference for yield prediction, irrigation optimization, and saline-land management in the Ningxia Yellow River irrigation district and comparable salinized regions. Future improvements should address process-variable validation, growth-stage stress sensitivity, and broader regional applicability.

(5) Simulated water–salt dynamics and stress patterns revealed three major inefficiencies in the current uniform four-irrigation schedule: persistent early-season stress at high-salinity sites, late-season salt accumulation at low-salinity sites, and a common K_stress trough during the tasseling–silking stage. These findings support the need for salinity-differentiated irrigation management and highlight the model's value as a decision-support tool for irrigation optimization in salinized farmland.

Declarations

Funding

This study was funded by the Ningxia Natural Science Foundation (Excellent Youth Project, Grant No. 2024AAC05048).

Competing Interests

The authors have no relevant financial or non-financial interests to disclose.

Data Availability

The datasets generated and/or analyzed during the current study are available from the corresponding author on reasonable request.

Code Availability

The code used for data analysis in this study is available from the corresponding author on reasonable request.

Author Contributions

J. Zhang designed the study, developed the coupled model, performed the data analysis, and wrote the manuscript. X. Shen supervised the research, provided funding, and revised the manuscript. R. Wu, J. Ji, and F. Shang assisted with field sampling and experimental data processing. All authors read and approved the final manuscript.

References

Allen RG, Pereira LS, Raes D, Smith M (1998) Crop evapotranspiration: guidelines for computing crop water requirements. FAO Irrigation and Drainage Paper No. 56. FAO, Rome

Balasubramaniam T, Shen G, Esmaeili N, Zhang H (2023) Plants' response mechanisms to salinity stress. Plants 12(12):2253. https://doi.org/10.3390/plants12122253

Cai F, Mi N, Ji RP et al (2019) Determination and performance evaluation of WOFOST model parameters based on spring maize field experiments at Jinzhou. Chin J Ecol 38:1238–1248 (in Chinese with English abstract). https://doi.org/10.13292/j.1000-4890.201905.030

Cao Y, Zhou X, Song H, Zhang M, Jiang C (2023) Advances in deciphering salt tolerance mechanism in maize. Crop J 11:1001–1010. https://doi.org/10.1016/j.cj.2022.12.004

Chen N, Li X, Šimůnek J et al (2022) Optimization of winter irrigation management for salinized farmland using a coupled model of soil water flow and crop growth. Agric Water Manag 272:107845. https://doi.org/10.1016/j.agwat.2022.107845

Chevuru S, Schmitz O, de Jong SM et al (2025) Feedbacks between water availability and crop systems using a coupled model. Hydrol Earth Syst Sci 29:4219–4239. https://doi.org/10.5194/hess-29-4219-2025

de Wit A, Boogaard H, Fumagalli D et al (2019) 25 years of the WOFOST cropping systems model. Agric Syst 168:154–167. https://doi.org/10.1016/j.agsy.2018.06.018

Dong Z, Jiang M, Xue X et al (2022) The applicability evaluation and drought validation of the WOFOST model for the simulation of winter wheat growth in Shandong Province, China. Heliyon 8:e12004. https://doi.org/10.1016/j.heliyon.2022.e12004

Feddes RA, Kowalik PJ, Zaradny H (1978) Simulation of field water use and crop yield. Centre for Agricultural Publishing and Documentation, Wageningen

Haj-Amor Z, Araya T, Kim DG et al (2022) Soil salinity and its associated effects on soil microorganisms, greenhouse gas emissions, crop yield, biodiversity and desertification: a review. Sci Total Environ 843:156946. https://doi.org/10.1016/j.scitotenv.2022.156946

Hao YY, Xu X, Ren DY et al (2015) Distributed simulation of soil water–salt dynamics and crop yield in the Hetao irrigation district using the HYDRUS–EPIC model. Trans CSAE 31(11):110–116 (in Chinese with English abstract). https://doi.org/10.11975/j.issn.1002-6819.2015.11.016

He M, Shen C, Peng S et al (2024) The influence of soil salinization, induced by the backwater effect of the Yellow River, on microbial community dynamics and ecosystem functioning in arid regions. Environ Res 262:119854. https://doi.org/10.1016/j.envres.2024.119854

Hopmans JW, Qureshi AS, Kisekka I et al (2021) Critical knowledge gaps and research priorities in global soil salinity. Adv Agron 169:1–191. https://doi.org/10.1016/bs.agron.2021.03.001

Huang JX, Jia SL, Ma HY et al (2017) Dynamic simulation of winter wheat growth in major production regions of China based on the WOFOST model. Trans CSAE 33(10):222–228 (in Chinese with English abstract). https://doi.org/10.11975/j.issn.1002-6819.2017.10.029

Islam MS, Islam MR, Hasan MK et al (2024) Salinity stress in maize: consequences, tolerance mechanisms, and management strategies. OBM Genetics 8(2):232. https://doi.org/10.21926/obm.genet.2402232

Jin JX, Ding YM, Sun ZY et al (2023) Simulation of spring wheat growth and yield in arid regions based on SWAP-IES. Trans CSAE 39(11):66–76 (in Chinese with English abstract). https://doi.org/10.11975/j.issn.1002-6819.202212080

Li P, Ren L (2021) Evaluating the saline water irrigation schemes using a distributed agro-hydrological model. J Hydrol 594:125688. https://doi.org/10.1016/j.jhydrol.2021.125688

Li X, Tan J, Li H et al (2023) Sensitivity analysis of the WOFOST crop model parameters using the EFAST method and verification of its adaptability in the Yellow River Irrigation Area, Northwest China. Agronomy 13(9):2294. https://doi.org/10.3390/agronomy13092294

Li XM, Zhang ZY, Yang JW et al (2022a) Characterization of soil salinization and its driving factors in a typical irrigation area of Northwest China. Sci Total Environ 837:155804. https://doi.org/10.1016/j.scitotenv.2022.155804

Li Y, Kinzelbach W, Zhou J et al (2012) Modelling irrigated maize with a combination of coupled-model simulation and uncertainty analysis, in the northwest of China. Hydrol Earth Syst Sci 16:1465–1480. https://doi.org/10.5194/hess-16-1465-2012

Li Y, Šimůnek J, Wang S et al (2023a) Quantifying water and salt movement in a soil–plant system of a corn field using HYDRUS (2D/3D) and the stable isotope method. Agric Water Manag 288:108500. https://doi.org/10.1016/j.agwat.2023.108500

Li Y, Xu X, Hu M et al (2023b) Modeling water–salt–nitrogen dynamics and crop growth of saline maize farmland in Northwest China: searching for appropriate irrigation and N fertilization strategies. Agric Water Manag 282:108274. https://doi.org/10.1016/j.agwat.2023.108274

Liu Z, Gao M, Sun Q et al (2023a) Formation and evolution of soil salinization based on multivariate statistical methods in Ningxia Plain, China. Front Earth Sci 11:1186779. https://doi.org/10.3389/feart.2023.1186779

Maas EV, Hoffman GJ (1977) Crop salt tolerance—current assessment. J Irrig Drain Div 103(IR2):115–134. https://doi.org/10.1061/JRCEA4.0001137

Miao Q, Yu D, Shi H et al (2025) Modeling sunflower yield and soil water–salt dynamics with combined fertilizers and irrigation in saline soils using APSIM and deep learning. Environ Sci Eur 37:104. https://doi.org/10.1186/s12302-025-01145-2

Mualem Y (1976) A new model for predicting the hydraulic conductivity of unsaturated porous media. Water Resour Res 12:513–522. https://doi.org/10.1029/WR012i003p00513

Munns R, Tester M (2008) Mechanisms of salinity tolerance. Annu Rev Plant Biol 59:651–681. https://doi.org/10.1146/annurev.arplant.59.032607.092911

Niu Z, Wang L, Qi T et al (2023) Soil salinization characteristics in irrigation region of Yellow River of Hongsipu, Ningxia. Arid Zone Res 40(11):1785–1796. https://doi.org/10.13866/j.azr.2023.11.08

Pan JL, Fan XW, Li YZ (2023) Insights into physio-biochemical responses of maize to salt shock stress and removal of the stress at the whole-plant level. Tropical Plants 2:20. https://doi.org/10.48130/TP-2023-0020

Saltelli A (2002) Making best use of model evaluations to compute sensitivity indices. Comput Phys Commun 145:280–297. https://doi.org/10.1016/S0010-4655(02)00280-1

Siad SM, Iacobellis V, Zdruli P et al (2019) A review of coupled hydrologic and crop growth models. Agric Water Manag 224:105746. https://doi.org/10.1016/j.agwat.2019.105746

Šimůnek J, van Genuchten MTh, Šejna M (2016) Recent developments and applications of the HYDRUS computer software packages. Vadose Zone J 15(7):1–25. https://doi.org/10.2136/vzj2016.04.0033

Šimůnek J, van Genuchten MTh (2008) Modeling nonequilibrium flow and transport processes using HYDRUS. Vadose Zone J 7:782–797. https://doi.org/10.2136/vzj2007.0074

Singh A (2022) Soil salinity: a global threat to sustainable development. Soil Use Manag 38:39–67. https://doi.org/10.1111/sum.12772

Sobol IM (1993) Sensitivity estimates for nonlinear mathematical models. Math Model Comput Exp 1:407–414

Tian Y, Bai Y, Liu J et al (2025) Estimating maize root zone soil moisture by assimilating high spatiotemporal resolution optical and radar remote sensing into the WOFOST–HYDRUS coupled model. J Hydrol 646:132618. https://doi.org/10.1016/j.jhydrol.2024.132618

van Dam JC, Groenendijk P, Hendriks RFA et al (2008) Advances of modeling water flow in variably saturated soils with SWAP. Vadose Zone J 7:640–653. https://doi.org/10.2136/vzj2007.0060

van Genuchten MTh (1980) A closed-form equation for predicting the hydraulic conductivity of unsaturated soils. Soil Sci Soc Am J 44:892–898. https://doi.org/10.2136/sssaj1980.03615995004400050002x

Van Keulen H, Wolf J (1986) Modelling of agricultural production: weather, soils and crops. Pudoc, Wageningen

Wang W, Jing H, Guo X et al (2023b) Analysis of water and salt spatio-temporal distribution along irrigation canals in Ningxia Yellow River irrigation area, China. Sustainability 15(16):12114. https://doi.org/10.3390/su151612114

Wang X, Huang G, Shi H et al (2017) Evaluating the effects of irrigation water salinity on water movement, crop yield and water use efficiency by means of a coupled hydrologic/crop growth model. Agric Water Manag 185:13–26. https://doi.org/10.1016/j.agwat.2017.01.012

Wang Y, Deng C, Liu Y et al (2024) Integrated drip irrigation regulates soil water–salt movement to improve water use efficiency and maize yield in saline–alkali soil. Water 16:2509. https://doi.org/10.3390/w16182509

Wang Y, Gao M, Chen H et al (2023a) Soil moisture and salinity dynamics of drip irrigation in saline-alkali soil of Yellow River basin. Front Environ Sci 11:1130455. https://doi.org/10.3389/fenvs.2023.1130455

Willmott CJ (1982) Some comments on the evaluation of model performance. Bull Am Meteorol Soc 63:1309–1313. https://doi.org/10.1175/1520-0477(1982)063<1309:SCOTEO>2.0.CO;2

Xing'an, Zhuo ZQ, Zhao YZ et al (2020) EFAST-based sensitivity analysis of WOFOST model parameters under different production levels. Trans CSAM 51(2):161–171 (in Chinese with English abstract). https://doi.org/10.6041/j.issn.1000-1298.2020.02.018

Xu X, Shen S, Xiong S et al (2021) Water stress is a key factor influencing the parameter sensitivity of the WOFOST model in different agro-meteorological conditions. Int J Plant Prod 15:231–242. https://doi.org/10.1007/s42106-021-00137-5

Zhai Y, Huang M, Zhu C et al (2022) Evaluation and application of the AquaCrop model in simulating soil salinity and winter wheat yield under saline water irrigation. Agronomy 12(10):2313. https://doi.org/10.3390/agronomy12102313

Zhang HL, Liu MH, Cai F et al (2026) Simulation of spring maize yield in northeast China by integrating data assimilation and the WOFOST model. Trans CSAE 42(4):206–215 (in Chinese with English abstract)

Zhang X, Zhao Y, Zhao Z et al (2023) A method for estimating yield of maize inbred lines by assimilating WOFOST model with Sentinel-2 satellite data. Front Plant Sci 14:1201179. https://doi.org/10.3389/fpls.2023.1201179

Zhao L, Zhang HR, Zhao XB et al (2025) Simulation of the soil water content under different water deficits for apple trees via improved WOFOST–HYDRUS coupled model. Int J Agric Biol Eng 18(1):219–229. https://doi.org/10.25165/j.ijabe.20251801.9384

Zhou J, Cheng GD, Li X et al (2012) Numerical modeling of wheat irrigation using coupled HYDRUS and WOFOST models. Soil Sci Soc Am J 76:648–662. https://doi.org/10.2136/sssaj2010.0467